Available online at www.sciencedirect.com
ScienceDirect
International Journal of Solids and Structures 44 (2007) 1768–1786
INTERNATIONAL JOURNAL OF SOLIDS and STRUCTURES
www.elsevier.com/locate/ijsolstr

Rupture mechanisms in combined tension and shear—Experiments

Imad Barsoum, Jonas Faleskog *

KTH Solid Mechanics, Royal Institute of Technology, SE-100 44 Stockholm, Sweden

Received 26 April 2006; received in revised form 26 September 2006
Available online 1 October 2006

Abstract

An experimental investigation of the rupture mechanisms in a mid-strength and a high-strength steel were conducted employing a novel test configuration. The specimen used was a double notched tube specimen loaded in combined tension and torsion at a fixed ratio. The effective plastic strain, the stress triaxiality and the Lode parameter were determined in the centre of the notch at failure. Scanning electron microscopy of the fractured surfaces revealed two distinctively different ductile rupture mechanisms depending on the stress state. At high stress triaxiality the fractured surfaces were covered with large and deep dimples, suggesting that growth and internal necking of voids being the governing rupture mechanism. At low triaxiality it was found that the fractured surfaces were covered with elongated small shear dimples, suggesting internal void shearing being the governing rupture mechanism. In the fractured surfaces of the high-strength steel, regions with quasi-cleavage were also observed. The transition from the internal necking mechanism to the internal shearing mechanism was accompanied by a significant drop in ductility.

Keywords: Ductile fracture; Rupture mechanisms; Experiments; Tension, Shear

1. Introduction

Ductile fracture governed by void growth and coalescence depends strongly on stress triaxiality (Van Stone et al., 1985, Garrison and Moody, 1987). The final phase in this fracture process is the link-up of voids (coalescence). At least two distinctly different mechanisms have been observed for this phase (see a recent discussion by Pardoen and Brechet, 2004): (i) internal necking down of ligaments between voids that have enlarged their sizes significantly, and (ii) internal shear localization of plastic strain in the ligaments between voids that have experienced limited growth. Mechanism (i) dominates at high stress triaxiality and mechanism (ii) at low stress triaxiality. At intermediate levels of triaxiality, these mechanisms may co-operate or even compete. In this study we experimentally investigate the two mechanisms and the conditions that governs the transition between them. It will be shown that ductility is significantly affected by the mechanism that is prevailing.

* Corresponding author. Tel.: +46 8 790 8977; fax: +46 8 411 2418.
E-mail address: jonasf@hallf.kth.se (J. Faleskog).

0020-7683/$ - see front matter
doi:10.1016/j.ijsolstr.2006.09.031

To quantify the influence of stress triaxiality on ductility Hancock and Mackenzie (1976) carry out experiments on smooth and notched round bars in three different low-alloy steels. Ductility is determined as the effective plastic strain required to initiate fracture. The experimental trend they observe: increasing ductility with decreasing stress triaxiality is rationalized by use of the theoretical models for void growth by McClintock (1968) and Rice and Tracey (1969). Clausing (1970), Speich and Spitzig (1982) and Hancock and Brown (1983) compare ductility from tests on notched plane strain specimens with notched round bars. They all note that the ductility typically is less for plane strain specimens than for axisymmetric specimens. One reason being that a plane strain specimen is more susceptible to plastic shear localization than what a axisymmetric specimen is, due to the kinematic constraints associated with overall axisymmetric deformation. McClintock (1971) compare effective plastic strain to fracture in tension and torsion in several different materials (see Table III in McClintock, 1971). For a majority of the materials the effective plastic strain to fracture is greater in tension than in torsion despite the lack of triaxiality in torsion. In a recent experimental investigation, Bao and Wierzbicki (2004a,b) employ several different specimen geometries (both plane strain and axisymmetric types) to cover stress triaxiality in the low to intermediate range. Their purpose is to explore several common models for ductility that are based on stress triaxiality. They conclude that none of the models are able to capture the behavior in the entire triaxiality range. Thus, the experimental observations discussed so far indicate that stress triaxiality is not enough to fully describe ductility.

In this study, the stress state will be characterized by use of the stress triaxiality, T, and the Lode parameter, μ. The Lode parameter plays the role of a deviatoric state parameter and is related to the third deviatoric stress invariant. T and μ are defined as

$$T = \frac{\sigma_\mathrm{h}}{\sigma_\mathrm{e}}, \qquad \mu = \frac{2\sigma_2 - \sigma_1 - \sigma_3}{\sigma_1 - \sigma_3}, \tag{1}$$

where σ_h is the mean stress, σ_e is the von Mises effective stress, and σ_1, σ_2 and σ_3 are the principal stresses with $\sigma_1 \geqslant \sigma_2 \geqslant \sigma_3$. These two parameters adequately describe the state of stress during plastic deformation for an isotropic material. The Lode parameter is illustrated by use of the Mohr circle in Fig. 1, where also the three special cases: generalized tension ($\mu = -1$), generalized shear ($\mu = 0$) and generalized compression ($\mu = 1$) are

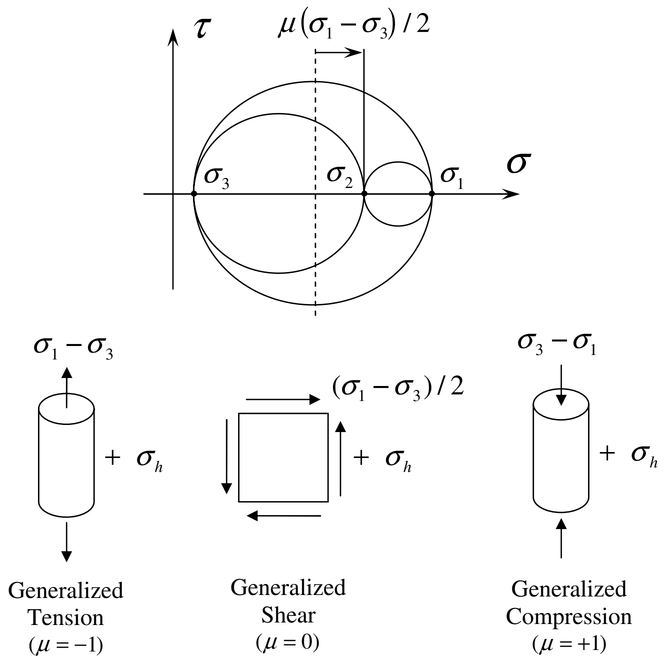

Fig. 1. Illustration of the Lode parameter μ and the three special cases: generalized tension, shear and compression, respectively. Here, σ_h denotes the superimposed hydrostatic stress equal to σ_3 for $\mu = -1$, σ_2 for $\mu = 0$ and σ_1 for $\mu = 1$, respectively.

shown. In the center of a notched round bar $\mu = -1$ and in the notched region of a plane strain specimen $\mu \approx 0$, provided that a tensile load is applied.

The influence of the Lode parameter on void growth and coalescence has to some extent been investigated in recent studies by Zhang et al. (2001), Kim et al. (2004) and Gao and Kim (2006). The effect of the Lode parameter is especially noticeable at lower values of stress triaxiality. Wierzbicki et al. (2005) propose a ductile failure criterion based on T and a deviatoric parameter related to μ. The outcome of the experimental results in Bao and Wierzbicki (2004a) is fairly well captured by their model.

In the present study, a new type of specimen—a double notched tube specimen—was developed and employed to carry out experiments in the low to intermediate triaxiality regime. The tube is loaded in combined tension and torsion giving rise to variations of the Lode parameter in the range $-1 \leqslant \mu \leqslant 0$. Two materials were tested. One intermediate strength, intermediate hardening material and one high strength, low hardening material.

The aim of this study was to experimentally determine the effective plastic strain at fracture (ductility) in terms of the parameters T and μ, and associate the behavior with the two different mechanisms in the void link-up process (coalescence) discussed above. Especially the conditions that govern the transition between the two mechanisms was of interest. The plan of the paper is as follows: in Section 2 the mechanical and microstructural properties of the two materials are given, in Section 3 the experimental setup and procedure, respectively, are described, and in Section 4 the experimental outcome is presented and discussed. To determine the type of mechanisms that governs final rupture, fractographical examinations of most fractured specimens were undertaken, which is shown in Section 5. The paper is concluded in Section 6.

2. Materials

Two materials were investigated, Weldox 420 and Weldox 960. The former material is a hot rolled medium-strength steel and the latter material is a quenched and annealed high-strength steel. Both materials were delivered in 30 mm thick plates. The chemical compositions of the two materials are listed in Table 1.

2.1. Mechanical properties

Uniaxial tests on smooth round bar specimens, with the tensile axis oriented in the rolling direction L of the plate, were performed for both the materials and the test data were fitted to the model in Eq. (2). For both materials Young's modulus E and Poisson's ratio ν were about 208 GPa and 0.3, respectively. All material and model parameters are listed in Table 2, where $R_{p0.2}$ is the 0.2% offset yield strength, R_m is the ultimate tensile strength and $\bar{\varepsilon}_f^p$ is the effective plastic strain at failure in the neck. The uniaxial test data from the two materials are shown in Fig. 2. For higher strain levels Bridgman correction was employed to compensate for the non uniform stress distribution due to necking. In Eq. (2), σ_0 represents the initial yield stress, ε_s an offset strain, ε_N a normalizing strain and $\varepsilon_0 = \sigma_0/E$.

$$\sigma = \begin{cases} E\varepsilon & \varepsilon \leqslant \varepsilon_0 \\ \sigma_0 & \varepsilon_0 \leqslant \varepsilon \leqslant \varepsilon_s + \varepsilon_N \\ \sigma_0\left(\dfrac{\varepsilon - \varepsilon_s}{\varepsilon_N}\right)^N & \varepsilon > \varepsilon_s + \varepsilon_N \end{cases}. \tag{2}$$

Table 1
Chemical composition of Weldox 420 and Weldox 960 given in weight%

Material	C	Si	Mn	S	Al	Mo	Ni	N
Weldox 420	0.14	0.50	1.70	0.015	0.015	0.05	0.10	0.015
Weldox 960	0.20	0.50	1.60	0.010	0.018	0.70	2.00	0.015

Table 2
Material parameters for the mechanical properties of Weldox 420 and Weldox 960

Material	$R_{p0.2}$ (MPa)	R_m (MPa)	$\bar{\varepsilon}_f^p$	σ_0 (MPa)	N	ε_0	ε_s	ε_N
Weldox 420	415	525	1.42	418	0.18	0.0020	0.0084	0.0162
Weldox 960	996	1051	1.27	956	0.059	0.0046	0	0.0046

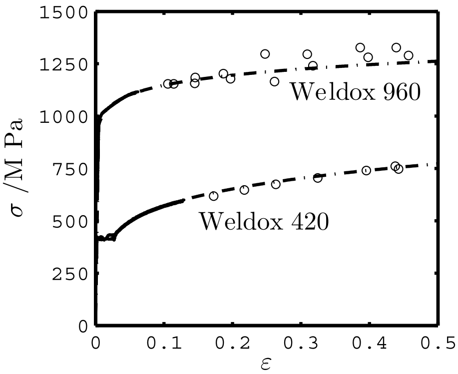

Fig. 2. The stress–strain curve of the uniaxial test for Weldox 420 and Weldox 960. The solid line is the experimental data, hollow circles Bridgman corrected data and dot-dashed line the power law fit according to Eq. (2).

2.2. Microstructural properties

The materials were also examined in a light microscope in order to obtain information such as inclusion sizes and microstructural features. This was done on sections cut perpendicular to the rolling direction L from a virgin material, which was polished before analyzed in the light microscope. The images were then imported into an image analysis software where the inclusions could be measured. The resolution allowed for inclusion measurements larger than about 1 μm in diameter, and thus sub-micron sized particles could not be detected. However, sub-micron sized particles, like e.g., cementite particles, were observed in examinations by scanning electron microscope.

In both materials, the inclusions consisted mainly of MnS, Al_2O_3 and SO_2 particles and were found to be of spherical shape. However, larger inclusions deviated from the spherical shape. Fig. 3 shows representative micrographs for both materials. The average inclusion diameters were 6.7 μm for Weldox 420 and 7.3 μm

a

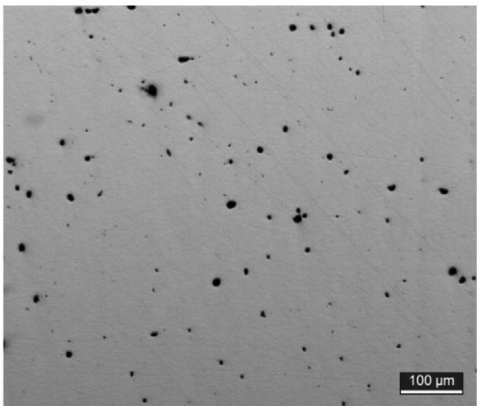

b

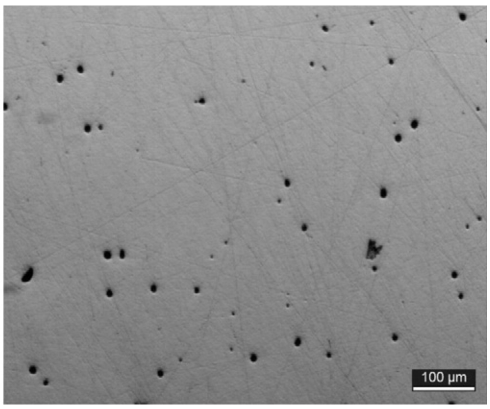

Fig. 3. Micrographs of polished surfaces taken from cross sections perpendicular to the rolling direction L, (a) Weldox 420 and (b) Weldox 960. The scale is indicated by a 100 μm distance.

for Weldox 960. The size distribution was such that 95% of all inclusions were less than 16.6 μm for Weldox 420 and 14.3 μm for Weldox 960. Finally, the inclusion surface fractions were estimated to be 0.88% for Weldox 420 and 0.60% for Weldox 960.

The sections were then etched in order to obtain the microstructure of the materials. Due to the different heat treatment methods the two materials will show different microstructural features. It was found that the hot rolled Weldox 420 has a banded ferrite/pearlite microstructure, where pearlite is the more brittle and ferrite the more ductile constituent. This banded structure renders its mid strength and increased ductile characteristics. The quenched and annealed Weldox 960 has however a bainitic/martensitic microstructure giving the material its high strength and a decreased ductility.

3. Experiments

The main objective of the experimental work was to gain a thorough understanding of the change in the ductile behavior with respect to the stress state. For this reason the stress triaxiality, the Lode parameter and the effective plastic strain at failure were of primary interest. The aim here was to characterize the different ductile mechanisms leading to ductile fracture. At high triaxiality the governing ductile rupture mechanism is internal necking of voids whereas at lower triaxiality the dominating rupture mechanisms is internal shearing of voids. Hence, of particular interest was to characterize the transition between these two rupture mechanisms.

3.1. Specimen

Tests were performed on circumferentially double notched tube specimens subjected to a combination of tensile and torsional loading, see Fig. 4(b). The tensile force and the torsional moment are here denoted N and M, respectively. The specimen dimensions are seen in Fig. 4(b and c), where the height $H = 120$ mm, the average tube radius as well as the radius to the centre of the notch $r_m = 12$ mm, the thickness of the tube $2t = 3.2$ mm, the net section thickness at the notch $2t_n = 1.2$ mm and the notch height $h = 1.0$ mm. The cur-

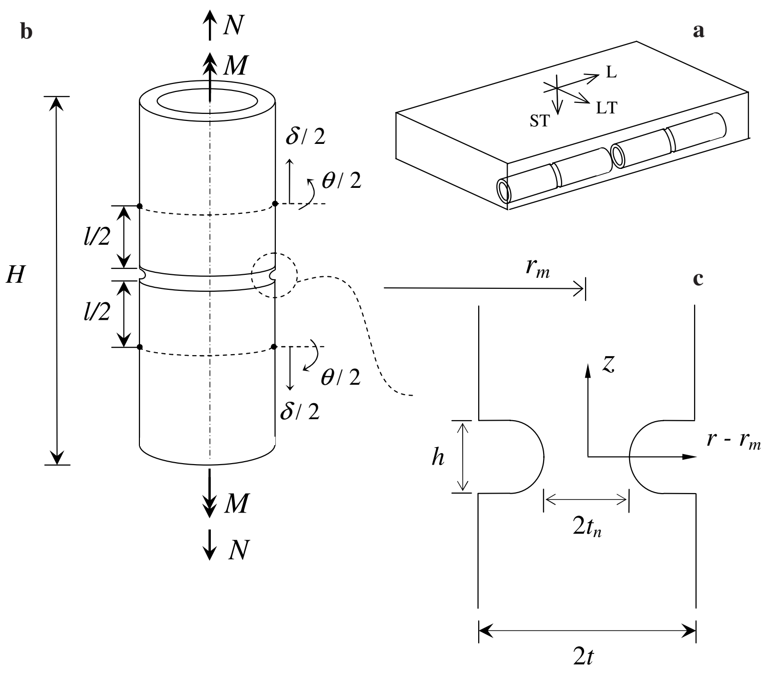

Fig. 4. (a) The orientation of the specimen with respect to the rolled plate. Specimens were cut in the longitudinal rolling direction L. (b) Configuration of the double notched tube specimen with (c) a close up of an axisymmetric cut of the notch.

rent geometrical configuration of the specimen was optimized to obtain as uniform stress distribution as possible in the symmetry plane ($z = 0$) of the notch. The specimens where cut from 30 mm thick plates so that the symmetry axis of the tube specimens was parallel to the longitudinal rolling direction L, as shown in Fig. 4(a).

The average normal stress and average shear stress over the cross section of the notch during loading are statically determined as $\sigma_n = N/(2\pi r_m 2t_n)$ and $\tau_n = M/(2\pi r_m^2 2t_n)$. All experiments were carried out keeping the ratio σ_n/τ_n constant. A load ratio parameter is introduced for this purpose as

$$\kappa = \frac{\sigma_n}{\tau_n} = \frac{N r_m}{M}. \tag{3}$$

By varying κ the stress triaxiality in the notch region can be controlled. Increasing values of κ implies more axial tension and thus a higher triaxiality, whereas decreasing κ values implies more torsional loading and thus a lower triaxiality.

3.2. Experimental setup

The tests were carried out with a universal servo-hydraulic material testing machine (MTS) with an Instron 8800 digital controller. The machine, seen in Fig. 5(a), allows for a combination of tension and torsion simultaneously. For high κ values, the proportional loading was achieved by applying a sufficiently low, constant piston axial displacement rate, monitoring the corresponding axial force N and then correcting it with an increment in the rotation of the piston giving an increase in torque M such that the ratio between N and M was kept constant according to Eq. (3). For low κ values on the other hand, this was done by applying a sufficiently low, constant piston rotation rate, monitoring M and then correcting it with an increment in the axial displacement of the piston giving an increase in N such that κ was kept constant. This correction procedure was done 10 times per second.

The axial displacement near the notch region was monitored by attaching two extensometers on fixture-rings (Fig. 5(c)) fixed to the specimen at a distance $(l + h)/2 = 13$ mm above and below the symmetry plane of the notch shown in Fig. 4(b). The axial displacement δ was then taken as the average of the acquired values of the two extensometers, which were placed at opposite sides on the specimen as can be seen in Fig. 5(c). The rotation θ was obtained from a clip gauge, which was mounted between the two flanges of the fixture-rings, as

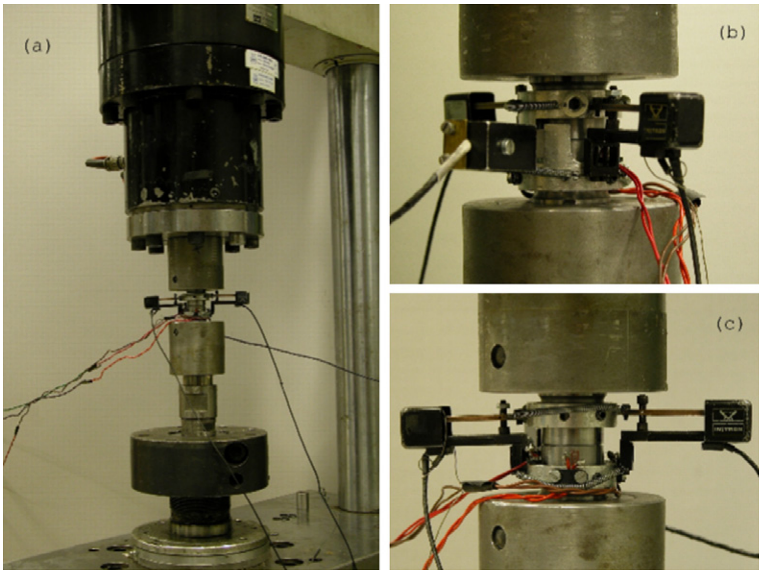

Fig. 5. (a) The specimen mounted in the MTS machine used for the combined tension-torsion experiment, (b) the clip gauge for the rotation measurements to the left and (c) the extensometers for the axial displacement measurements.

shown to the right in Fig. 5(b). By measuring the relative displacement of the two flanges, the rotation could be determined.

In order to check the circumferential variation in axial stress due to possible misalignments of the specimen in the testing machine, three strain gauges were used in each test. The strain gauges were glued on the outside of the tube, 120° apart at the circumference, and at a distance of about 9 mm (=9h) from the notch. By monitoring the strain and assuming that linear elastic conditions prevailed remote from the notch, the circumferential variation in the axial stress could be estimated during a test. The strain was monitored with the digital acquisition system Orion, which was synchronized with the Instron 8800 digital controller.

3.3. Evaluation of the stress state in the notch

The stress state in the notch region was carefully calculated by analyzing all the tests by use of the finite element program ABAQUS (2004). A very detailed two-dimensional model of the double notched tube specimen was used. A special 2D generalized axisymmetric 8 node element with an additional degree of freedom corresponding to the twist angle was employed to allow for the deformation modes of the applied load of combined tension and torsion. The material was assumed to be elasto-plastic with isotropic hardening according to Eq. (2) and a finite strain J_2 flow theory was employed.

For both materials the load-deformation response from the finite element analysis were in good agreement with the experimental results, as can be seen in Fig. 6. In this figure the finite element and the experimental results are compared for a test on Weldox 960 with $\kappa = 1.03$. Thus, the finite element simulations of the experiments were considered to be a reliable tool for prediction of the state in the notched region.

3.4. Evaluation of the effective plastic strain in the notch

The effective plastic strain was evaluated by assuming that all plastic deformation is confined to and solely takes place in the notch region. This is an accurate assumption, as also will be seen in Section 4, since the notch is relatively deep, $(t - t_n)/t = 0.625$. Furthermore, it was assumed that the displacement δ and rotation θ, measured over the distance $l + h$, can be additively decomposed into their respective elastic and plastic parts. Hence, the plastic deformation over the notch can be expressed as

$$\delta_n^p = \delta - C_\delta N, \quad \theta_n^p = \theta - C_\theta M, \tag{4}$$

where $C_\delta = \Delta\delta/\Delta N$ and $C_\theta = \Delta\theta/\Delta M$ are the elastic compliances in tension and torsion, respectively. These compliances were directly estimated from the linear part of the load-deformation records during a test, as illustrated in Fig. 6. The average logarithmic normal and shear plastic strain rates over the notch region with current extension $h + \delta_n$ then becomes

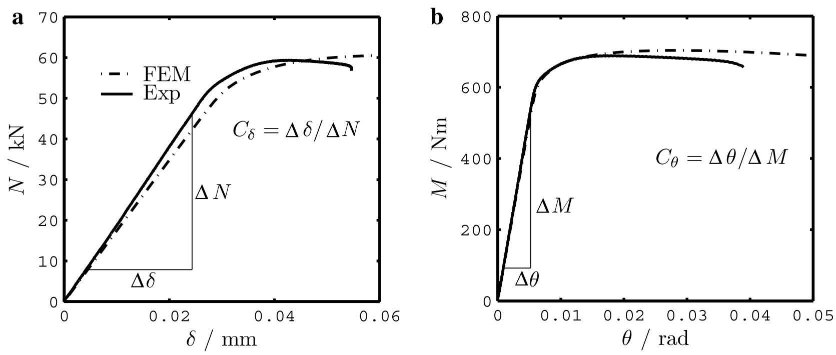

Fig. 6. Comparison of the load-deformation response over the region $l + h$ between the experiment and the finite element simulation for Weldox 960 with $\kappa = 1.03$. (a) The axial force N vs. the axial displacement δ and (b) the torsional moment M vs. the rotation θ. Here C_δ and C_θ are the tension and torsion elastic compliances estimated from experimental results.

$$\dot{\varepsilon}_{\mathrm{n}}^{p}=\frac{\dot{\delta}_{\mathrm{n}}^{p}}{(h+\delta_{\mathrm{n}})},\quad \dot{\gamma}_{\mathrm{n}}^{p}=\frac{r_m\dot{\theta}_{\mathrm{n}}^{p}}{(h+\delta_{\mathrm{n}})}. \tag{5}$$

In the denominators, δ_{n} is the total axial displacement over the notch. The total rotation over the notch is denoted θ_{n}. These will be expressed below.

Since the unnotched part of the tube specimen can be assumed to remain elastic during loading, the possibility of plastic flow in the circumferential direction in the notched region will be significantly constrained. The plastic strain was in this direction therefore neglected. This was also checked by finite element calculations and seemed to hold for the full range of triaxiality considered. The rate of effective plastic strain, averaged over the notch, can then be expressed as

$$\dot{\bar{\varepsilon}}_{\mathrm{n}}^{p}=\sqrt{\frac{4(\dot{\varepsilon}_{\mathrm{n}}^{p})^2+(\dot{\gamma}_{\mathrm{n}}^{p})^2}{3}}. \tag{6}$$

The accumulated effective plastic strain, averaged over the notch, is then obtained by integration of Eq. (6)

$$\bar{\varepsilon}_{\mathrm{n}}^{p}=\int\dot{\bar{\varepsilon}}_{\mathrm{n}}^{p}\mathrm{d}t. \tag{7}$$

The elastic compliances, as depicted in Fig. 6, are the sum of the contributions from the notched region (subscript n) and unnotched region (subscript l). By using this, the total axial displacement and the total rotation over the notch can be evaluated as

$$\delta_{\mathrm{n}}=\delta-\frac{C_\delta}{1+C_{\delta\mathrm{n}}/C_{\delta\mathrm{l}}}N,\quad \theta_{\mathrm{n}}=\theta-\frac{C_\theta}{1+C_{\theta\mathrm{n}}/C_{\theta\mathrm{l}}}M. \tag{8}$$

Approximate expressions for the compliance ratios, $C_{\delta\mathrm{n}}/C_{\delta\mathrm{l}}$ and $C_{\theta\mathrm{n}}/C_{\theta\mathrm{l}}$, can be derived if uniaxial conditions are assumed and the notch is modeled as a cylinder with average radius r_m and average thickness $2\bar{t}_{\mathrm{n}}$, where $2\bar{t}_{\mathrm{n}}=2.36t_{\mathrm{n}}$ is the average notch thickness accounting for the notch radius. Straight forward calculations then give that $C_{\delta\mathrm{n}}/C_{\delta\mathrm{l}}=(ht)/(l\bar{t}_{\mathrm{n}})$ and $C_{\theta\mathrm{n}}/C_{\theta\mathrm{l}}=[ht(1+(t/r_m)^2)]/[l\bar{t}_{\mathrm{n}}(1+(\bar{t}_{\mathrm{n}}/r_m)^2)]$. The same ratios were also estimated by finite element calculations and in summary we obtain:

$$\text{Approximate}: C_{\delta\mathrm{n}}/C_{\delta\mathrm{l}}=0.0901,\quad C_{\theta\mathrm{n}}/C_{\theta\mathrm{l}}=0.0914, \tag{9}$$

$$\text{FEM}: C_{\delta\mathrm{n}}/C_{\delta\mathrm{l}}=0.0614,\quad C_{\theta\mathrm{n}}/C_{\theta\mathrm{l}}=0.0835. \tag{10}$$

In the evaluation of expressions in Eq. (8) the ratios in Eq. (10) were used.

Fig. 7 shows a comparison of $\bar{\varepsilon}_{\mathrm{n}}^{p}$ evaluated from experimental load-deformation records using Eqs. (4)–(8) and (10) with $\bar{\varepsilon}_{\mathrm{n}}^{p}$ computed in the same way using results from a finite element simulation of the corresponding test. Results from three different tests, $\kappa=1.03$, 3.47 and 5.73, on Weldox 960 are included in the figure. The

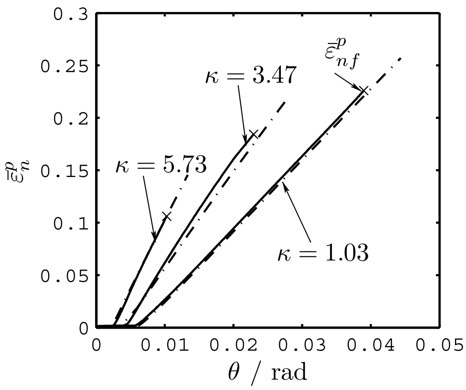

Fig. 7. The average effective plastic strain $\bar{\varepsilon}_{\mathrm{n}}^{p}$ in the notch vs. the rotation θ for three different tests on Weldox 960. Solid lines represent experiments and dot-dashed lines FEM simulations.

agreement between the curves is remarkably good in all three cases. The experimental curves all terminate at the point of failure, marked with a cross. The average effective plastic strain over the notch at this instance is denoted $\bar{\varepsilon}^p_{\mathrm{nf}}$.

3.5. Range in triaxiality and Lode parameter

The possible range in triaxiality was examined by finite element calculations as described above, where the load ratio was varied from pure shear ($\kappa = 0$) to pure tension ($\kappa = \infty$). Since, most of the progressing damage leading to material failure and onset of ductile fracture occurred in the centre part of the symmetry plane of the notch, T and μ were examined at this location, i.e., $r = r_m$ and $z = 0$. Fig. 8(a) shows the relation between T and κ for Weldox 420 and Weldox 960. Each material is represented by two curves. The T- and κ-values for each curve are evaluated at a fixed value of $\bar{\varepsilon}^p_{\mathrm{n}}$, as indicated in the figure. The chosen $\bar{\varepsilon}^p_{\mathrm{n}}$-values cover the relevant span in failure strain for both materials. The maximum attainable triaxiality is about 1.15–1.20 for Weldox 420 and about 1.30–1.35 for Weldox 960. The planning of the experimental program was based on the information in Fig. 8(a). In order to perform a test with a desired triaxiality, the load ratio, κ, was chosen according to Fig. 8(a).

Fig. 8(b) shows the variation of the Lode parameter with triaxiality. Again each material is represented by two curves, where T- and μ-values are evaluated at fixed $\bar{\varepsilon}^p_{\mathrm{n}}$-values. At low and high triaxiality, the stress approaches a state of generalized shear ($\mu \to 0$). In between the stress approaches a state of generalized tension

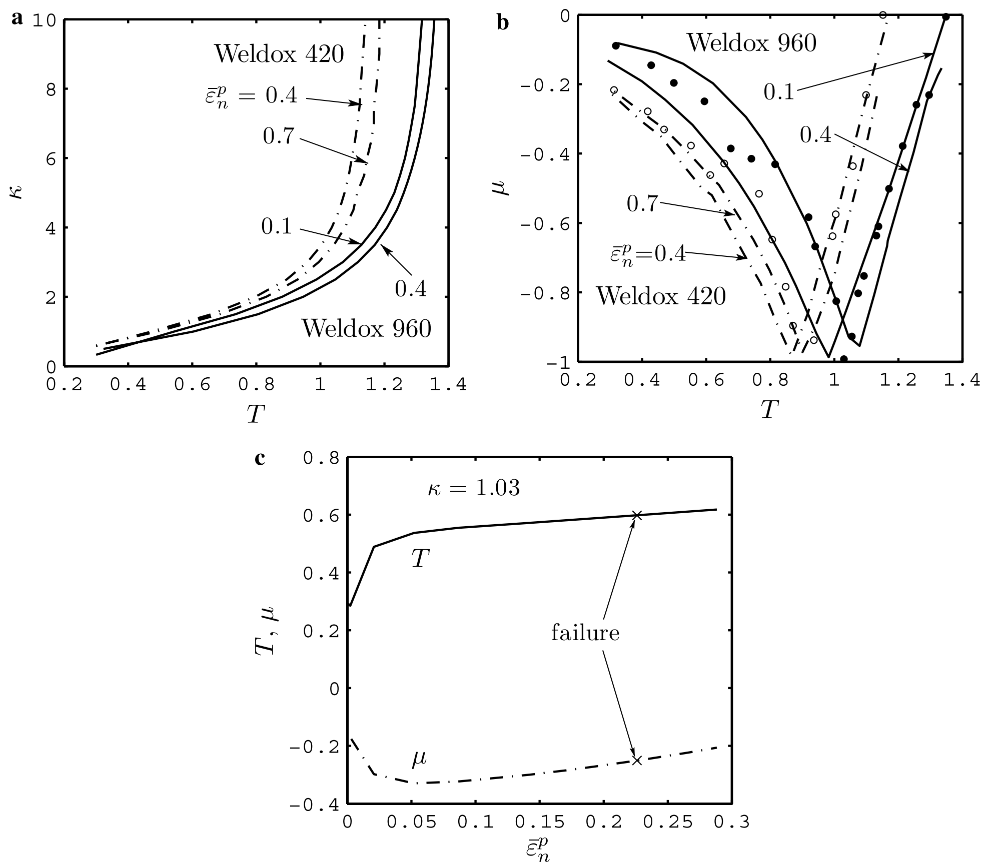

Fig. 8. (a) κ vs. T and (b) μ vs. T evaluated at two different values of $\bar{\varepsilon}^p_{\mathrm{n}}$ for each of the materials Weldox 420 (dot-dashed lines) and Weldox 960 (solid lines), respectively. In (b), the open symbols (Weldox 420) and solid symbols (Weldox 960) are experimental data evaluated at failure. (c) T and μ vs. $\bar{\varepsilon}^p_{\mathrm{n}}$ for a test on Weldox 960 with $\kappa = 1.03$. All data in (a), (b) and (c) pertain to the centre of the notch ($r = r_m$, $z = 0$).

($\mu \to -1$). The curves are very similar for both materials, but the curves pertaining to Weldox 960 are shifted somewhat to the right.

The V-shaped relation between μ and T seen in Fig. 8(b) can qualitatively be explained as discussed below, and for this purpose we make use of the coordinate system defined in Fig. 4(c). At low T-values, shear deformation prevails in the notch and the normal strains ε_r, ε_φ and ε_z are small compared to the shear strain $\gamma_{\varphi z}$. And thus the stress state can be characterized as close to generalized shear, i.e., $\mu \approx 0$. For this case, the strain in the thickness direction of the notch, ε_r, corresponds to the middle principle strain. At high T-values, the directions of the principle strains coincide with the axis of the $r\varphi z$-coordinate system. For this case, the strain in the circumferential direction, ε_φ, is negligible and the strain in the r-direction, ε_r, is equal to the smallest principle strain. Again, the stress state can be characterized as close to generalized shear, and $\mu \approx 0$. At this juncture, it should be noted that the strain in the thickness direction, ε_r, always can be identified as the middle or the smallest of the principle strains. As the triaxiality increases from lower to higher values, ε_r changes from being the middle to being the smallest principle strain. At that instance the middle and the smallest principle strains are equal, indicative of the axisymmetric stress state of generalized tension as shown in Fig. 1, and μ is expected to be close to -1.

The evolution of T and μ in the centre of the notch during the load history is shown in Fig. 8(c), where $\bar{\varepsilon}^p_{\mathrm{n}}$ is used as the load parameter. It can be observed that both T and μ are rather constant between $\bar{\varepsilon}^p_{\mathrm{n}} = 0.05$ and the failure strain, $\bar{\varepsilon}^p_{\mathrm{nf}} = 0.23$. This span in $\bar{\varepsilon}^p_{\mathrm{n}}$ covers the important part of the load history. This particular case belongs to Weldox 960 with $\kappa = 1.03$. However, the situation is very similar for the whole triaxiality range and both materials. For instance the T-value at failure only exceeds the average T-value during the load history by at most 5–10%.

3.6. Accuracy of stress state estimation

In Section 3.2 it was mentioned that a set of three strain gauges was used to monitor a possible circumferential variation in axial stress due to misalignment of the specimen in the testing machine. How the measurements from the strain gauges were used to estimate variations in axial stress are described in some detail in the Appendix A. From these measurements it was concluded that the relative variation in axial stress in most tests were 7% or less.

4. Results

A series of 16 specimens were tested of the material Weldox 420 and a series of 21 specimens were tested of the material Weldox 960. The tests were performed with a range of κ-values to obtain a carefully chosen interval in triaxiality based on Fig. 8(a). The stress triaxiality T and the Lode parameter μ were determined in the centre of the notch at the failure point as indicated in Fig. 8(c). In these experiments the failure event is preceded by a very rapid rupture process, which is characterized by a sudden load drop. In most cases, except for tests with $T < 0.4$, a crack initiated at this moment leading to instant fracture and separation of the two specimen halves. For the tests with $T < 0.4$, the initiated crack propagated through a large part of the cross section in the circumference and arrested at some point. Total separation was then achieved by pulling the two specimen halves apart. For tests with higher triaxiality, examination of the fracture surfaces revealed development of shear lip zones in the regions near the notch roots. In tests with low triaxiality, the fracture surfaces from Weldox 420 were flat, whereas the surfaces from Weldox 960 showed a flat zig zag pattern in the circumferential direction. The flat feature of the fracture surfaces at low triaxiality was presumably a consequence of the uniform stress state in between the notch roots as will be shown below in Fig. 9(a).

4.1. General behavior

It is assumed that fracture initiates in the centre portion of the notch, therefore it is of interest to examine the spatial variation of T, μ and the effective plastic strain, $\bar{\varepsilon}^p$. The full field solutions obtained by the finite element calculations described in Section 3.3 were used for this purpose. First, the variations through the thickness in the symmetry plane ($z = 0$) will be explored. In Fig. 9, T, μ and $\bar{\varepsilon}^p$ are plotted at failure for three

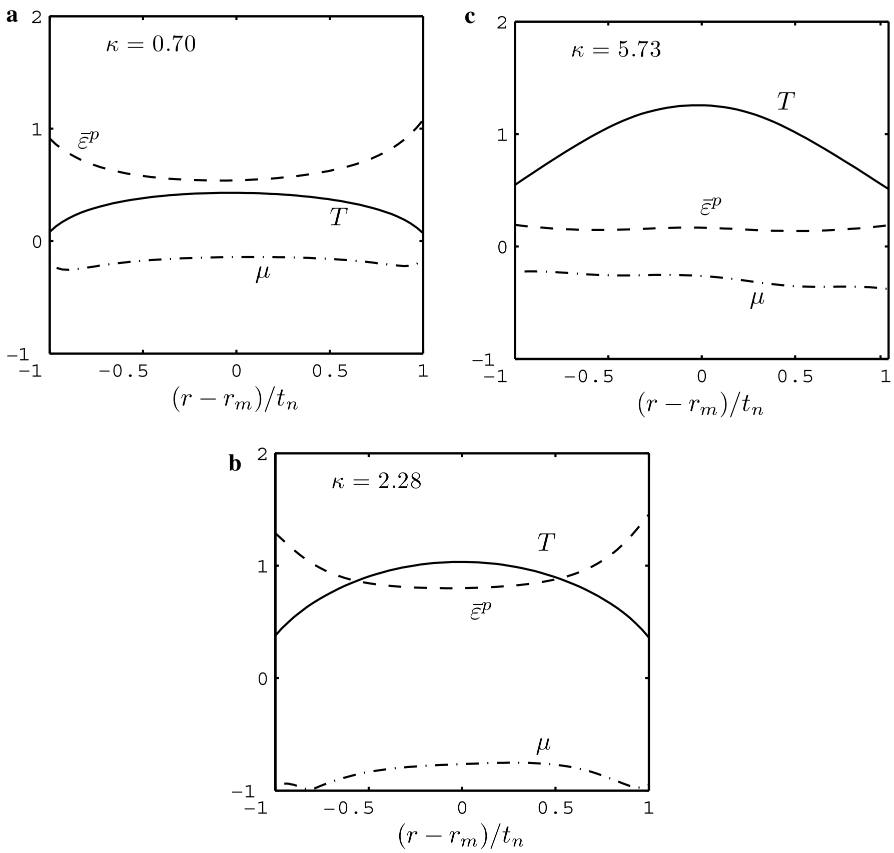

Fig. 9. The stress state and the effective plastic strain at failure vs. the normalized distance through the thickness at the symmetry plane ($z = 0$) for Weldox 960. (a) $\kappa = 0.70$, (b) $\kappa = 2.28$ and (c) $\kappa = 5.73$.

different tests for Weldox 960. These tests correspond to κ-values covering the relevant span of triaxiality investigated here. It can be seen that the stress state is rather uniform in the mid-portion of the notch for all the three cases. In all cases the effective plastic strain $\bar{\varepsilon}^p$ is highest at the notch roots $(r - r_m)/t_\mathrm{n} = \pm 1$ and decreases toward the centre of the notch at $(r - r_m)/t_\mathrm{n} = 0$, whereas the trend for the triaxiality T is the opposite. The Lode parameter μ is however rather constant through the thickness. The overall trends in thickness variations are very similar for both materials.

In Fig. 10 iso-contours of T, μ and $\bar{\varepsilon}^p$ are shown for Weldox 960 with $\kappa = 2.28$ at failure. Due to symmetry in the axial direction only the upper half of the notch region is shown. As can be seen in Fig. 10(a), the Lode parameter μ shows little variation in the axial direction in the notch region. Not shown here, the iso-contours of the Lode parameter for both lower and higher κ-values also shows little variation in the axial direction at failure. The triaxiality however in Fig. 10(b) exhibits a more marked variation in the axial direction, with decreasing T away from the notch centre. Again not shown here, this behavior is similar for higher κ-values whereas for lower κ-values the triaxiality is rather constant in the axial direction. The iso-contours of the effective plastic strain are shown in Fig. 10(c) indicating that the plastic deformation is confined to the notched region as assumed in Section 3.4. Furthermore, the high levels of $\bar{\varepsilon}^p$ is localized to the symmetry plane ($z = 0$). Similar behavior is found for higher and lower κ-values.

4.2. Failure locus

To construct a relevant failure locus for each material, it is desired to determine the effective plastic strain at failure in the centre of the notch, $\bar{\varepsilon}^p_\mathrm{cf}$, as discussed in Section 3.4. This is done by relating $\bar{\varepsilon}^p_\mathrm{c}$ to $\bar{\varepsilon}^p_\mathrm{n}$ by use of the

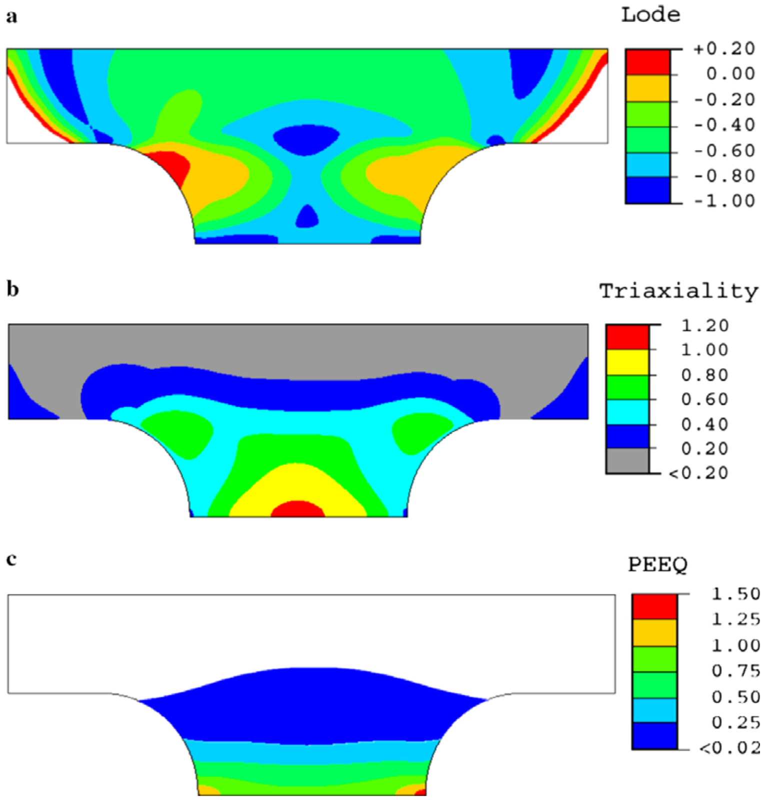

Fig. 10. Contour plots of the notch region (undeformed configuration) at failure for Weldox 960 with $\kappa = 2.28$. (a) Lode parameter μ, (b) stress triaxiality T and (c) effective plastic strain $\bar{\varepsilon}^p$ (denoted PEEQ above).

finite element results and extracting $\bar{\varepsilon}^p_{\rm cf}$ at the corresponding $\bar{\varepsilon}^p_{\rm nf}$ determined from the experiments. Fig. 11 shows the results from three tests carried out on Weldox 960 representing a wide span of triaxiality levels. Here, the failure points are indicated with cross-markers. Note that the relation between $\bar{\varepsilon}^p_{\rm c}$ and $\bar{\varepsilon}^p_{\rm n}$ seems to be rather independent of κ, all three curves fall close together.

The effective plastic strains at failure, $\bar{\varepsilon}^p_{\rm nf}$ and $\bar{\varepsilon}^p_{\rm cf}$, are plotted versus the stress triaxiality, T, at failure in Fig. 12. Here the solid circles represent $\bar{\varepsilon}^p_{\rm nf}$ and the open circles represent $\bar{\varepsilon}^p_{\rm cf}$. The lines are simple curve fits

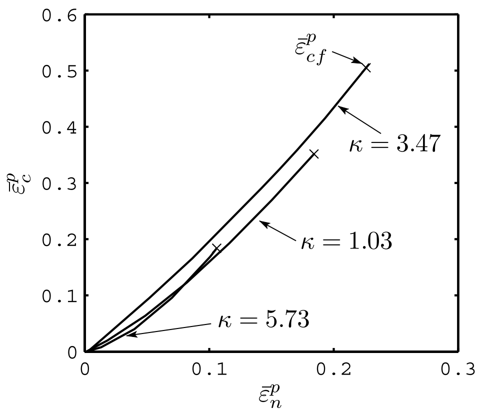

Fig. 11. The effective plastic strain $\bar{\varepsilon}^p_{\rm c}$ in the centre of the notch vs. the average effective plastic strain $\bar{\varepsilon}^p_{\rm n}$ over the notch for Weldox 960, where $\bar{\varepsilon}^p_{\rm cf}$ denotes the effective plastic strain in the centre of the notch at failure.

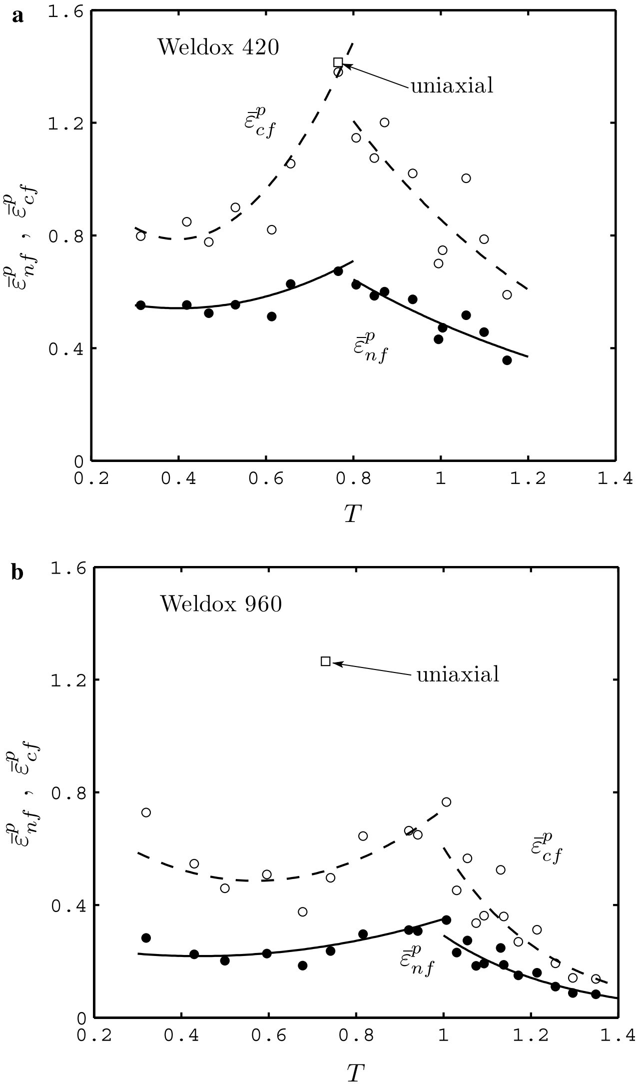

Fig. 12. The effective plastic strain at failure vs. stress triaxiality T, where solid circles denote $\bar{\varepsilon}^p_{\rm nf}$ and open circles denote $\bar{\varepsilon}^p_{\rm cf}$. The open squares pertain to results from uniaxial tests on smooth round bars. (a) Weldox 420 and (b) Weldox 960.

to emphasize the trends in the failure loci. Both materials exhibit similar behavior. In the high triaxiality regime, the failure strain increases with a decrease in triaxiality as could be expected from void growth and coalescence driven failure models (cf. McClintock, 1968 and Rice and Tracey, 1969). As the triaxiality decreases this behavior changes abruptly, indicating a transition in the rupture mechanism. This occurs at $T = 0.8$ for Weldox 420 and $T = 1.0$ for Weldox 960. With a further decrease in triaxiality beyond this point, the failure strain starts to decrease until it appears to reach a plateau value.

For reference purposes, the effective plastic strain at failure from the uniaxial tensile tests on smooth round bar specimens (Table 2 above) are also included in Fig. 2. Due to axisymmetry, the Lode parameter $\mu = -1$ in the centre of a round bar specimen. The stress triaxiality values in these tests were estimated according to Bridgman (1964), giving $T = 0.76$ for Weldox 420 and $T = 0.73$ for Weldox 960. Contrary to what was observed in the double notched tube specimen, T varied significantly in a round bar specimen during a uniaxial test due to necking. Therefore, the uniaxial tests were also analyzed by use of finite element modeling, which revealed that the T-values based on Bridgman (1964) are close to the mean value of T during the load history (Weldox 420: 0.64 and Weldox 960: 0.79). The T-value at failure is as high as

1.02 for Weldox 420 and 1.16 for Weldox 960 in the centre of the smooth round bar specimen. Returning to Fig. 12, it is interesting to note the uniaxial data of Weldox 420 virtually coincide with the transition point mentioned above, whereas the uniaxial data of Weldox 960 appears to fit into the $T - \bar{\varepsilon}^p_{\mathrm{cf}}$ trend of the high triaxiality regime if extrapolated to lower T-values. Additionally, the tests on the uniaxial round bars seem to yield higher ductility than what can be obtained with the present tube specimen. This difference is more noticeable for the high strength Weldox 960 steel. A similar trend is reported by Clausing (1970) (cf. Fig. 3 in his paper).

In Fig. 8(b) the symbols pertain to the Lode parameter μ versus stress triaxiality T at failure for each test. At low and high triaxiality the stress state is close to generalized shear ($\mu \approx 0$), whereas a state of generalized tension ($\mu \approx -1$) is reached in between. The shift between a decreasing and an increasing μ value as T increases is rather sharp. This shift is seen to occur at about $T = 1.0$ for Weldox 960 (filled circles in Fig. 8(b)), which coincides with the abrupt change in the $T - \bar{\varepsilon}^p_{\mathrm{cf}}$ behavior for this material as previously observed from Fig. 12(b). For Weldox 420, which is denoted by open circles in Fig. 8(b), this shift occurs at about $T = 0.9$. The abrupt change in the $T - \bar{\varepsilon}^p_{\mathrm{cf}}$ behavior for Weldox 420 occurs at the slightly lower stress triaxiality $T = 0.8$, as shown in Fig. 12(a).

Some data of interest from the experiments are summarized in Table A.1 in Appendix A. Note, that the relative variation in the load ratio parameter κ is typically around 5%. In a few cases, especially at low triaxiality, higher values can be noted. The last column in the tables shows the ratio $\bar{\varepsilon}^p_{\mathrm{n}}/\bar{\gamma}^p_{\mathrm{n}}$ at failure. This ratio is fairly constant during the load history. Interestingly, the ratio remains small (<0.3) for T-values to the left of the transition region in ductility, cf. Fig. 12. This indicates that the mode of deformation is dominated by plastic shearing.

5. Fractography

An extensive scanning electron microscopic (SEM) study was undertaken in order to asses the underlying ductile failure mechanisms in these materials at the different stress triaxiality levels. A systematic examination of most of the fracture surfaces was done. The surfaces were primarily scanned in the regions around $\varphi = \varphi_0 + \pi/2$ and $\varphi = \varphi_0 - \pi/2$, see Fig. A.1 in Appendix A. These are regions where maximum and minimum triaxiality are expected to occur. However, no major differences between these two regions were found in the fractographs.

5.1. Weldox 420—moderate-strength steel

In Fig. 13, the three fractographs represent the rupture mechanisms at low triaxiality (a), high triaxiality (c) and at the triaxiality where the transition in failure strain was seen to occur in Fig. 12(a).

Fig. 13(a) ($T = 0.47$) clearly shows that the failure mode is shear ductile rupture. This mode is characterized by shallow small elongated shear dimples, which are oriented along the shear direction. Wearing resulting from contact between the two separated fracture surfaces can also be observed. This rupture mode involves internal shearing between voids and is favored at lower triaxiality. The high plastic strain level promote nucleation of voids at the second phase particles and inclusions by particle cracking or interface decohesion. The low triaxiality impedes growth of the formed voids, which undergo substantial shearing. The final rupture is then caused by the internal void shearing mechanism.

Fig. 13(c) ($T = 1.10$) reveals a distinctly different failure mode. The fracture surface here exhibits large deep dimples. The growth of the formed voids is substantial and is promoted by the high stress triaxiality. The void growth dominates the failure process until the deformation localizes, and the large voids coalesce by reduction of the intervoid ligament, which necks down and lead to rupture. The final rupture is then caused by the internal void necking mechanism. Some of the voids have grown to a diameter of approximately 15 μm. In contrast, the voids in the shear dimple mode in Fig. 13(a) are significantly smaller with sizes less than 5 μm.

The fractograph in Fig. 13(b) ($T = 0.85$), taken from the transition region, shows a mixture of the two failure modes discussed above. The dimples are however not as elongated as in (a) and not as deep and large as in (c). Evidently, the two competing failure mechanisms involve different size scales of voids.

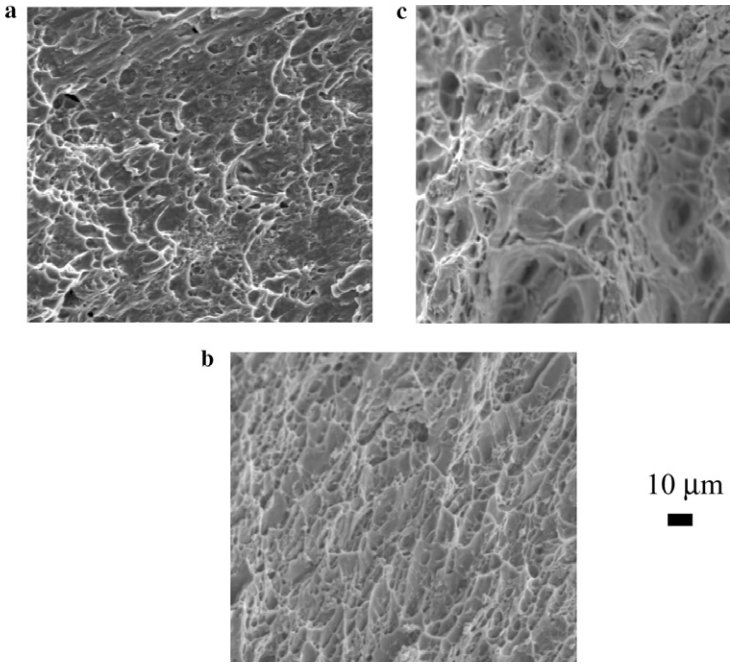

Fig. 13. SEM fractographs showing the rupture modes for Weldox 420. In (a) with $T = 0.47$ shows the shear dimple rupture mode where the predominant failure mechanism is the intervoid shearing mechanism. In (c) with $T = 1.10$, shows the flat dimple rupture mode where the governing failure mechanism is necking of intervoid ligament, whereas (b) where $T = 0.85$ is at the transition region.

5.2. Weldox 960—high-strength steel

A similar set of fractographs as presented in the section above are shown in Fig. 14 for Weldox 960. The rupture mode characteristics at high triaxiality ($T = 1.24$) for the internal void necking mechanism can be observed in Fig. 14 (c). However, at low triaxiality ($T = 0.32$) as shown in Fig. 14(a), the mode of rupture differs to some extent from the behavior observed in Weldox 420 at low triaxiality. In this martensitic/bainite quenched high-strength steel, the shear type fracture surface reveal quasi-cleavage features blended into areas with small shear dimples. A similar behavior is observed in high-strength steels by Knott (1980). In Fig. 14(b) ($T = 1.06$) it can be seen that the fracture surface exhibits a mix of the features observed in (a) and (c).

In summary, the shift in rupture mechanisms observed in the fractographical examination occur in the same triaxiality range as the trend shift in failure strain noted in Fig. 12. This is valid for both materials.

6. Conclusions

In this study a new specimen is developed and optimized to measure ductility in tension and shear. The specimen, a double notched tube, is loaded in a combined tensile and torsional loading at a fixed ratio allowing for control of the stress triaxiality. It was shown that the test and the evaluation procedure renders accurate results for estimation of the effective plastic strain and characterization of the stress state at failure. The stress state was characterized in terms of the stress triaxiality T and the Lode parameter μ, where the latter is a deviatoric stress state parameter. Two materials were investigated, a medium-strength steel $R_{p0.2} = 415$ MPa and a high-strength steel $R_{p0.2} = 996$ MPa.

It is well known that triaxiality has a strong influence on ductility. This was also confirmed in the current experimental study at sufficiently high triaxiality, where the rupture mechanism is characterized by void growth and coalescence. However, as the triaxiality decreases, which in the present study is accomplished by an increasing amount of shearing, a shift in rupture mechanism occurs. This shift in mechanism was confirmed by the fractographical examination conducted and accompanied with a dramatic change in the Lode

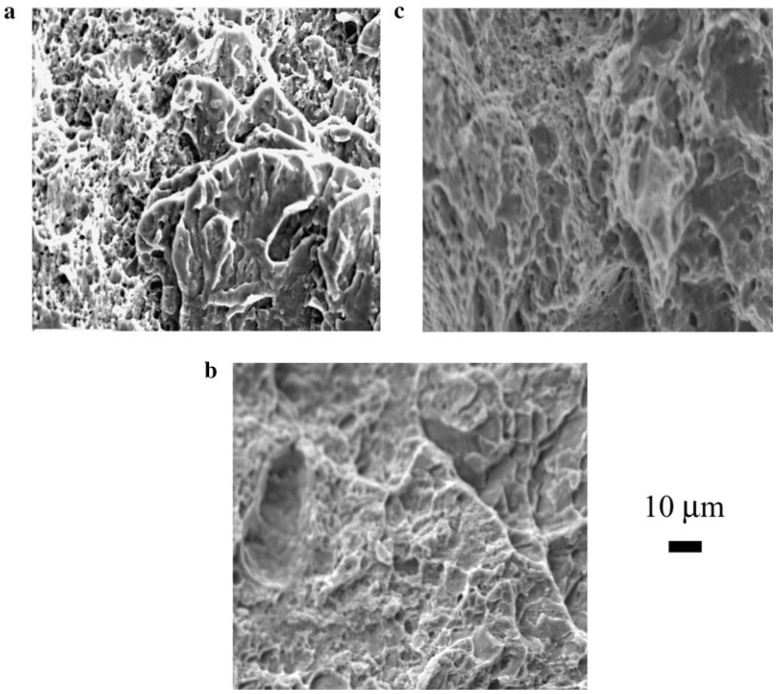

Fig. 14. SEM fractographs showing the rupture modes for Weldox 960. In (a) with $T = 0.32$ shows the shear dimple rupture mode where the predominant failure mechanism is the intervoid shearing mechanism with quasi-cleavage features. In (c) with $T = 1.24$, shows the flat dimple rupture mode where the governing failure mechanism is necking of intervoid ligament, whereas (b) where $T = 1.06$ is at the transition region.

parameter. Going from high to low triaxiality the rupture mechanism changed from internal necking to shearing between voids. This observation is valid for both the moderate and the high-strength steels tested here, suggesting that triaxiality is not a sufficient parameter to characterize ductility, especially at low levels of triaxiality. Bao and Wierzbicki (2004b), Wierzbicki et al. (2005) and Gao and Kim (2006) have also observed that predictions of ductile failure can be improved by introducing a deviatoric stress state parameter.

Alluding to an ongoing micromechanical study (Barsoum and Faleskog, 2006) of the experiments conducted here, it is found that the presence of voids do not seem to play a major role for predicting ductile failure at low levels of triaxiality. Instead failure seems to be governed by a simple criterion based on a critical measure of plastic shear deformation.

Acknowledgements

The authors acknowledge the financial support from the Swedish Research Council under contract 621-2004-5121. Mr. Hans Öberg is greatly acknowledged for developing the testing fixture and programming the testing machine. Messrs. Bertil Dolk, Martin Öberg, Bengt Möllerberg and Kurt Lindqvist are also acknowledged for manufacturing the specimens. Finally, Dr. Torbjörn Narström at SSAB Oxelösund is acknowledged for supplying the material used in this investigation.

Appendix A

Here it will be described how the measurements from the three strain gauges were used to estimate circumferential variations in the axial stress in the notch. Fig. A.1 shows the position of the strain gauges along the perimeter of the tube specimen, where the measured strains are denoted ε_1, ε_2 and ε_3. We assume that

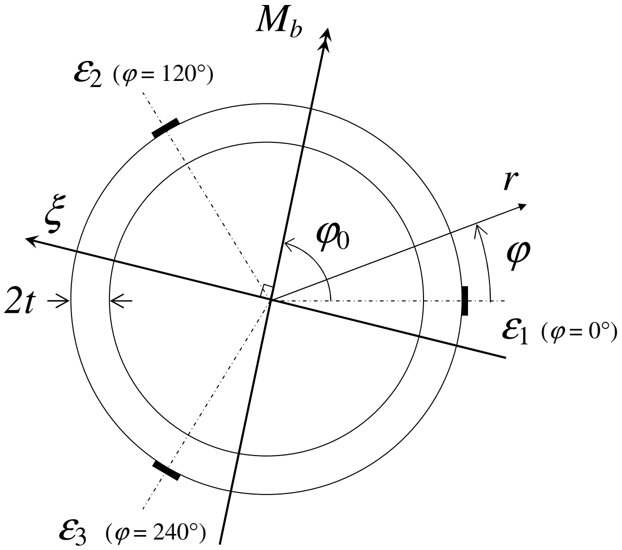

Fig. A.1. The strain gauges ε_1, ε_2 and ε_3 attached on the tube perimeter about a distance $9h$ away from the notch cross section.

the variation in axial strain along the perimeter, $\varepsilon(\varphi)$, is due to a curvature caused by a bending moment arising from misalignments. Then, if linear elastic conditions prevail

$$\varepsilon(\varphi) = \varepsilon_0 + \varepsilon_a \sin(\varphi - \varphi_0), \tag{A.1}$$

where the average normal strain ε_0 and the amplitude strain ε_a (due to bending) are given by

$$\varepsilon_0 = (\varepsilon_1 + \varepsilon_2 + \varepsilon_3)/3, \tag{A.2}$$

$$\varepsilon_a = \frac{2}{3}\sqrt{\varepsilon_1^2 + \varepsilon_2^2 + \varepsilon_3^2 - \varepsilon_1\varepsilon_2 - \varepsilon_1\varepsilon_3 - \varepsilon_2\varepsilon_3}. \tag{A.3}$$

In (A.1), the angle φ_0 defines the direction of the neutral axis of the bending moment. This angle may change during the loading history and can be calculated from the relation

$$\tan\varphi_0 = \frac{\varepsilon_2 + \varepsilon_3 - 2\varepsilon_1}{\sqrt{3}(\varepsilon_2 - \varepsilon_3)}. \tag{A.4}$$

The amplitude strain ε_a is directly connected to the maximum deviation of the normal stress along the perimeter of the notch, here denoted $\Delta\sigma_n$. Accounting for the deviation in the load ratio parameter, the ratio between the normal stress and the shear stress in the notch region as introduced in Section 3.1, becomes

$$\kappa \pm \Delta\kappa = \frac{\sigma_n \pm \Delta\sigma_n}{\tau_n} = \kappa\left(1 \pm \frac{\Delta\sigma_n}{\sigma_n}\right). \tag{A.5}$$

Note that the relative variation in the loading parameter $\Delta\kappa/\kappa$ is equal to $\Delta\sigma_n/\sigma_n$.

Bounds can be derived for $\Delta\sigma_n$ by considering two 'extreme' variations along the notch perimeter. An upper bound can be obtained by assuming a linear variation, i.e., $\xi\Delta\sigma_n$ (ξ is defined in Fig. A.1), and a lower bound can be obtained by assuming a bi-constant variation, i.e., $\pm\Delta\sigma_n$ for $\pm\xi$. The tensile force applied on the specimen can be related to the average strain in (A.2) as $N = \varepsilon_0 E(2\pi r_m 2t)$, and hence the average normal stress in the notch can be expressed as $\sigma_n = N/(2\pi r_m 2t_n) = \varepsilon_0 Et/t_n$. The bending moment caused by misalignment can be related to the amplitude strain in (A.3) as $M_b = \varepsilon_a E(\pi r_m^3 2t)/(r_m + t)$. Simple calculations then give the upper bound as: $\Delta\sigma_n = M_b/(\pi r_m^2 2t_n)$, and the lower bound as: $\Delta\sigma_n = M_b/(4r_m^2 2t_n)$. Finally, maximum of the relative variation in the load ratio parameter in the circumference of the notch becomes

Table A.1
Experimental data set for Weldox 420 and Weldox 960, where $_f$ indicates quantity at failure

Weldox 420					Weldox 960				
No.	κ	$\Delta\kappa/\kappa$	T	$(\bar{\varepsilon}_n^p/\bar{\gamma}_n^p)_f$	No.	κ	$\Delta\kappa/\kappa$	T	$(\bar{\varepsilon}_n^p/\bar{\gamma}_n^p)_f$
1	0.63	0.26	0.31	0.03	1	0.50	0.08	0.32	0.01
2	0.82	0.19	0.42	0.08	2	0.70	0.22	0.43	0.01
3	0.96	0.19	0.47	0.06	3	0.85	0.07	0.50	0.10
4	1.12	0.22	0.55	0.26	4	1.03	0.03	0.60	0.07
5	1.29	—	0.61	0.18	5	1.27	0.09	0.68	0.14
6	1.36	—	0.66	0.16	6	1.41	0.09	0.74	0.05
7	1.69	0.06	0.77	0.34	7	1.54	0.06	0.82	0.11
8	1.87	0.09	0.81	0.36	8	1.87	0.04	0.92	0.07
9	2.08	0.03	0.85	0.31	9	2.00	0.03	0.94	0.40
10	2.33	0.12	0.87	0.61	10	2.28	0.05	1.01	0.48
11	2.63	0.03	0.94	0.44	11	2.48	0.07	1.03	0.63
12	3.26	0.04	1.00	0.63	12	2.70	0.03	1.06	0.40
13	3.52	0.04	1.00	0.87	13	2.93	0.03	1.07	0.51
14	4.25	0.02	1.06	0.89	14	3.04	—	1.09	0.58
15	5.89	0.05	1.10	1.26	15	3.43	0.01	1.13	0.66
16	—	—	1.15	—	16	3.47	0.01	1.14	1.61
					17	3.93	0.03	1.17	0.55
					18	4.61	0.03	1.21	0.78
					19	5.73	0.01	1.26	0.97
					20	7.87	0.07	1.30	2.46
					21	—	—	0.70	—

The $\Delta\kappa$ values are for $k = 0.69$ in Eq. (A.6). In Experiment No. 5 and 6, for Weldox 420, and in Experiment No. 14, for Weldox 960, the strain gauges were out of function.

$$\frac{\Delta\kappa}{\kappa} = \frac{\Delta\sigma_n}{\sigma_n} = k\frac{\varepsilon_a}{\varepsilon_0}, \tag{A.6}$$

where $k = 1/(1 + t/r_m)$ for the upper bound and $k = (\pi/4)/(1 + t/r_m)$ for the lower bound. With the present geometry: $k = 0.88$ (upper bound) and $k = 0.69$ (lower bound). The maximum value of κ occurs at $\varphi = \varphi_0 + \pi/2$ with respect to strain gauge ε_1 (see Fig. A.1), and the minimum occurs at the opposite side at $\varphi = \varphi_0 - \pi/2$. Values of $\Delta\kappa/\kappa$ are for each test given in Table A.1.

Appendix B. Supplementary data

Supplementary data associated with this article can be found, in the online version, at doi:10.1016/j.ijsolstr.2006.09.031.

References

ABAQUS, 2004. Standard-User's Manual, Version 6.4. Hibbit, Karlsson and Sorensen, Inc., Providence, RI.

Bao, Y., Wierzbicki, T., 2004a. A comparative study on various ductile crack formation criteria. Journal of Engineering Materials and Technology 126, 314–324.

Bao, Y., Wierzbicki, T., 2004b. On the fracture locus in the equivalent strain and stress triaxiality space. International Journal of Mechanical Sciences 46, 81–98.

Barsoum, I., Faleskog, J., 2006. Rupture mechanisms in combined tension and shear—micromechanics. Submitted for publication.

Bridgman, P.W., 1964. Studies in large plastic flow and fracture. Harvard University Press, Cambridge, MA.

Clausing, D.P., 1970. Effect of plastic strain state on ductility and toughness. International Journal of Fracture Mechanics 6, 71–85.

Gao, X., Kim, J., 2006. Modeling of ductile fracture: significance of void coalescence. International Journal of Solids and Structures 43, 6277–6293.

Garrison Jr., W.M., Moody, N.R., 1987. Ductile fracture. Journal of Physics and Chemistry of Solids 48, 1035–1074.

Hancock, J.W., Brown, D.K., 1983. On the role of strain and stress state in ductile fracture. Journal of Mechanics and Physics of Solids 31, 1–24.

Hancock, J.W., Mackenzie, A.C., 1976. On the mechanisms of ductile failure in high-strength steels subjected to multi-axial stress-states. Journal of Mechanics and Physics of Solids 24, 147–169.

Kim, J., Gao, X., Srivatsan, T.S., 2004. Modeling of void growth in ductile solids: effects of stress triaxiality and initial porosity. Engineering Fracture Mechanics 71, 379–400.

Knott, J.F., 1980. Micromechanisms of fibrous crack extension in engineering alloys. Metal Science 14, 327–336.

McClintock, F.A., 1968. A criterion for ductile fracture growth of holes. Journal of Applied Mechanics 35, 363.

McClintock, F.A., 1971. Plasticity aspects of fracture. In: Fracture III, pp. 47–225.

Pardoen, T., Brechet, Y., 2004. Influence of microstructure-driven strain localization on the ductile fracture of metallic alloys. Philosophical Magazine 84, 269–297.

Rice, J.R., Tracey, D.M., 1969. On the ductile enlargement of voids in triaxial stress fields. Journal of Mechanics and Physics of Solids 17, 201–217.

Speich, G.R., Spitzig, W.A., 1982. Effect of volume fraction and shape of sulfide inclusions on through-thickness ductility and impact energy of high-strength 4340 plate steels. Metallurgical Transactions A 13A, 2239–2257.

Van Stone, R.H., Cox, T.B., Low, J.R., Psioda, J.A., 1985. Microstructural aspects of fracture by dimpled rupture. International Metals Reviews 30, 157–179.

Wierzbicki, T., Bao, Y., Lee, Y.W., Bai, Y., 2005. Calibration and evaluation of seven fracture models. International Journal of Mechanical Sciences 47, 719–743.

Zhang, K.S., Bai, J.B., Francois, D., 2001. Numerical analysis of the influence of the lode parameter on void growth. International Journal of Solids and Structures 38, 5847–5856.